This is a peer-reviewed, accepted author manuscript of the following research article: Metwly, MY, Ahmed, M, Hemeida, A, Abdel-Khalik, AS, Hamad, MS, Belahcen, A, Ahmed, S & Elmalhy, NA 2023, 'Investigation of six-phase surface permanent magnet machine with typical slot/pole combinations for integrated onboard chargers through methodical design optimization', IEEE Transactions on Transportation Electrification, vol. 9, no. 1, pp. 866-885. https://doi.org/10.1109/TTE.2022.3197451

Investigation of Six-Phase Surface Permanent Magnet Machine with Typical Slot/Pole Combinations for Integrated Onboard Chargers Through Methodical Design Optimization

Mohamed Y. Metwly, Graduate Student Member, IEEE, Mohamed Ahmed, Ahmed Hemeida, Ayman S. Abdel-Khalik, Senior Member, IEEE Mostafa S. Hamad, Senior Member, IEEE, Anouar Belahcen, Senior Member, IEEE, Shehab Ahmed, Senior Member, IEEE and Noha A. Elmalhy

***Abstract*—This paper presents an analytical magnetic equivalent circuit (MEC) modeling approach for a six-phase surface-mounted permanent magnet (SPM) machine equipped with fractional slot concentrated winding (FSCW) for integrated onboard chargers. For the sake of comparison, selected asymmetrical six-phase slot/pole combinations with the same design specifications and constraints are first designed based on the parametric MEC model and then optimized using a multi-objective genetic algorithm (MOGA). The commercial BMW i3 design specifications are adopted in this paper. The main focus of this study is to achieve optimal design of the SPM machine considering both the propulsion and charging performances. Thus, a comparative study of the optimization cost functions, including the peak-to-peak torque ripple and core losses under both motoring and charging modes and electromagnetic forces under charging, is conducted. In addition, the demagnetization capability in the charging mode and the overall cost of the employed machines are optimized. Since the average propulsion torque is crucial in electric vehicle (EV) applications, it is maintained through the design optimization process. Furthermore, finite element (FE) simulations have been carried out to verify the results obtained from the analytical MEC model. Eventually, the effectiveness of the proposed design optimization process is corroborated with experimental tests on a 2-kW prototype system.**

***Index Terms*—Electric vehicles; integrated on-board chargers; slot/pole combinations; finite element analysis (FEA); magnetic equivalent circuit (MEC); analytical modeling.**

I. INTRODUCTION

ELECTRIC vehicles (EVs), the optimal alternative to fossil-fueled vehicles, promote the emission-free future envisaged for the automotive industry since they utilize clean energy [1]. Therefore, governments provide financial subsidies to encourage the adoption of EVs to achieve climate goals. The global market share of EVs is highly growing and is expected to reach 230 million vehicles in 2030 [2]. The widespread adoption of EVs imposes vital challenges such as – low charging time and available charging points [3]. To overcome these challenges, integrated on-board battery chargers (OBCs) have been extensively introduced in the recent literature [4]. Integrated OBCs combine the charging process with the propulsion equipment, namely, electric machine and power converter, offering reduced space, weight, and cost of EVs when compared to conventional OBCs [3]. In [5], a single-phase integrated OBC that utilizes an active power filter (APF) and a bidirectional Quasi-Z-source converter has been elaborated. Another high-power three-phase integrated on-board charger that uses an additional interface converter has been presented in [6]. Moreover, a recent solution has been investigated based on DC charging [7].

The employed machine and the winding topology highly affect the charging performance of integrated battery chargers [8, 9]. Due to their high efficiency and power density, permanent magnet synchronous machines (PMSMs) are the most dominant electric machines used in EVs when compared to inductions motors (IMs) and switched-reluctance motors (SRMs) [10]. For instance, the Nissan Leaf and BMW i3 employ PMSMs, while Tesla models utilize IMs (e.g. Model S and Model X) [11]. SRMs are not among potential candidates for EV propulsion since the machine's torque ripple is quite high. Both three-phase and multiphase configurations can be used in integrated EVs charging applications [12, 13]. Multiphase machines offer inherent fault tolerant capability and improve torque density when compared to their three-phase counterparts. Besides, lower current rating per phase through

Mohamed Y. Metwly is with Smart-CI Center, Alexandria University, Alexandria, Egypt (email: m.metwly@smartci.alexu.edu.eg)

Mohamed Ahmed is with the Department of Mathematics and Applied Physics, Alexandria University, Alexandria, Egypt (email: mohamed.abuyehia@alexu.edu.eg)

Ahmed Hemeida is with the Department of Electrical Engineering, Cairo University, Giza, Egypt and Department of Electrical Engineering and Automation, Aalto University, FI-00076, Espoo, Finland (email: a.hemeida@cu.edu.eg and ahmed.hemeida @aalto.fi)

Ayman S. Abdel-Khalik and Noha A. Elmalhy are with the Department of Electrical Engineering, Alexandria University, Alexandria, Egypt (email: ayman.abdel-khalik@alexu.edu.eg and noha.elmalhy@alexu.edu.eg)

Mostafa S. Hamad is with the Department of Electrical and Control Engineering, Arab Academy for Science, Technology and Maritime Transport, Alexandria, Egypt (email: mostafa.hamad@staff.aast.edu)

Anouar Belahcen is with the Department of Electrical Engineering and Automation, Aalto University, FI-00076, Espoo, Finland (email: anouar.belahcen@aalto.fi)

Shehab Ahmed is with the CEMSE Division at King Abdullah University of Science and Technology, Saudi Arabia (email : shehab.ahmed@kaust.edu.sa)

(Corresponding author: Ayman S. Abdel-Khalik)

splitting the power across a higher number of phases [14]. Furthermore, multiphase machines ensure nullified average torque production owing to their higher degrees of freedom, the prime motivation to utilize the multiphase machine in the EV charging mode of operation.

From a manufacturing perspective, six-phase powertrain systems, namely the propulsion machine and the inverter, have been seen as the upcoming solution for commercial EVs [15]. Six-phase machines are advantageous over nine-phase counterparts in many ways. the realization is more practical with a charging power equal to the propulsion power while offering reduced heat sink requirements [16]. Furthermore, the simplified converter topology with a lower number of inverter modules as well as a modest controller with a reduced number of current controllers constitute the major advantages of six-phase systems. Considerable savings in the vehicles` cost, size, and weight are acquired.

Based on the available literature, PMSMs can adopt several winding configurations such as – integral-slot distributed winding (ISDW), integral-slot concentrated winding (ISCW), fractional slot distributed winding (FSDW) and fractional slot concentrated winding (FSCW) [10, 17]. Moreover, unconventional winding topology to avoid the rotor skew, i.e. 39-slot/12-pole, has been recently presented [18]. Most commercial EVs adopt the ISDW PMSM (e.g. 48-slot/8-pole [19] and 72-slot-12pole [20]). However, FSCW-based PM machines are considered as powerful candidates for EV applications owing to short-end turn, high slot fill factor, and flux weakening capability. Nevertheless, the distorted air gap flux distribution constitutes the main drawback of FSCW [21]. In [3], viable slot/pole combinations for EV applications are investigated under both propulsion and charging operational modes, shedding light on the induced eddy current rotor losses with respect to the employed winding layout. Compared to dual three-phase and symmetrical winding arrangements, the asymmetrical one gives minimum rotor loss index in the motoring mode. Thus, this study adopts the asymmetrical six-phase surface-mounted PM (SPM) machine with several slot/pole combinations.

Performance-wise, the main criteria when designing an SPM machine for the integrated charging process of EVs – besides the developed torque and core losses – are radial forces, irreversible demagnetization, and cost [22-25]. Even though considerable design optimization work has been reported in the literature, a concept satisfying all the above-mentioned objectives has not been conceived so far. Ref. [26] proposed a low-cost PM motor by combining a rare-earth PM with ferrite PM in the rotor, forming a hybrid PM excitation. Moreover, a multi-objective optimization method is used to investigate the design trade-off between five objectives of average output torque, cogging torque, PM cost, torque ripple, and efficiency. Accordingly, the feasibility of the less-rare-earth PM machine has been verified. Another crucial aspect when designing the PMSM is the irreversible demagnetization, which yields the deterioration in the performance of the motors [27, 28]. Rare-earth NdFeB magnets are well-known for their high residual magnetic flux density and coercivity; albeit, these magnets can be easily demagnetized at high temperatures [23]. Therefore, Ref. [23] presented the design optimization of PMSM considering the demagnetization characteristics. In that case, minimum demagnetization rate and maximum average torque constitute the objectives of the optimization problem, while the constraints are the peak-to-peak torque ripple and efficiency. As a result, the average torque and demagnetization rate were ameliorated by 2.7% and 4.45%, respectively.

Furthermore, the reduction in unbalanced magnetic pull (UMP) produced in SPM machines equipped with FSCW has been recently elaborated in [24]. The UMP highly affects the lifetime and performance of the motor [29]. Therefore, the design optimization of a 54-slot/48-pole SPM machine based on the Taguchi method [30] has been presented taking into consideration the improvement of PM shape of unequal thickness. In that case, the optimization problem aims at reducing the UMP and torque fluctuations. Thus, the operation stationarity is efficiently improved.

Even though most of the above-mentioned multi-objective optimization techniques were based on 2-D and 3-D finite element (FE) models, magnetic equivalent circuit (MEC) analytical models have been considered as an elegant alternative to FE ones in the recent literature [31, 32]. Although FE techniques offer higher accuracy when compared to parametric models, they require a heavy computational burden. Ref. [31] introduced a multi-objective optimization of an SPM machine based on the analytical MEC modelling approach. As a result, the optimization efficiency and torque performance are improved at a low computational time. Moreover, Ref. [8] introduced the design of a 12-slot/10-pole six-phase SPM based on the MEC model comparing the machine electromagnetic performance with several winding arrangements (i.e. dual three-phase and asymmetrical six-phase configurations). In the motoring mode, the asymmetrical six-phase layout has shown a superior performance from torque performance and core losses perspectives. However, under charging, the dual three-phase configuration has resulted in considerable forces. That's why the dual three-phase winding configuration is not recommended for integrated OBCs.

This paper presents a comprehensive study of viable FSCW slot/pole combinations that accommodate six-phase winding layouts under the integrated charging process of EVs. This paper extends the analysis presented in [3], at which the winding factor, lowest common multiple, greatest common divisor, and particularly the rotor loss index of several six-phase slot/pole combinations were discussed. It is worth mentioning that the design optimization of PM machines has been extensively addressed in the literature for EV traction applications; however, this study mainly focuses on the integrated EV charging application. Moreover, a comparison of the proposed design optimization approach with the ones presented in the literature has been introduced, as revealed in Table I. The main contributions are summarized as follows:

- Develop a design optimization of six SPM machines with the same ratings and constraints based on the analytical MEC model for integrated on-board EV battery charging.

- Formulate a multi-objective genetic algorithm (MOGA) optimization of the employed machines, where torque performances and core losses under the propulsion and charging modes are considered among the optimization objectives. The irreversible demagnetization under charging is considered as well, which has not been performed in previous studies.
- Study the effect of the selected FSCW slot/pole combination on the machine cost considering the stator core, rotor core, winding, and PM costs, a notable contribution of this study.
- Conduct FE simulations to verify the design optimization process and present the electromagnetic performance of the selected six slot/pole combinations.
- Build a prototype for a 2 kW 12-slot/10-pole SPM to further validate the design optimization process.

TABLE I. Comparison of design optimization methodologies.

Ref.	No. of phases	Slot/pole combination	Optimization algorithm/ method	Min torque ripple and core loss under propulsion	Min torque ripple and core loss under charging	Thermal demagnetization	Radial forces
[19]	6	18/8	No	Yes	No	Yes	No
[24]	3	54/48	Taguchi	Yes	No	No	Yes
[26]	3	12/10	SNP	Yes	No	Yes	No
[10]	3	Various	GA	Yes	No	Yes	Yes
[31]	6	48/44	MODE-RMO	Yes	No	No	No
[8]	6	12/10	LHS	Yes	Yes	No	Yes
[33]	6	12/10	MOGA	Yes	Yes	No	no
Prop.	6	Various	MOGA	Yes	Yes	Yes	Yes

* Latin hypercube samples (LHS) - multi-objective differential evolution with ranking-based mutation operator (MODE-RMO) - sequential nonlinear programming (SNP)

II. Integrated OBCs Employing Machines with FSCW

This section presents FSCW-based PM machines that can be utilized as the powertrain element of the integrated OBC. Initially, the theory of operation of the integrated OBC under both the propulsion and charging modes of operation is illustrated, shedding light on the operation requirements and safety standards. After that, various FSCW slot/pole combinations will be introduced based on the available literature. It is worth mentioning that considerable work has been done on the PM machines with FSCW in the motoring mode; however, the employment of several FSCW slot/pole combinations has not been investigated in the charging mode thus far. Therefore, design considerations of several six-phase SPM machines with FSCW are presented in this paper.

A. Theory Operation of Integrated OBC

Due to the limited power transfer capability of OBCs, the integrated on-board EV battery chargers have recently emerged as a compromise between the EV cost, volume, and weight while simultaneously offering a charging power at the same rated current [34-36]. Integrated OBCs reuse the powertrain elements, including the motor and inverter, in the charging process. The main challenge concerning the EV integrated chargers – besides minimal hardware reconfiguration to switch between the two operational modes and unity power factor operation at the grid side – is the average torque elimination. Therefore, multi-phase machines are preferred over their three-phase counterparts due to their higher degrees of freedom. Various operation and safety standards with respect to the EV charging process are demanded [1, 37]. For instance, the total harmonic distortion should be less than 7% according to IEEE-519-2014 standard [38], microgrid inverter standards during the bidirectional OBC operation according to IEEE-1547-2018 [39] and UL-1741 [40] standards, and battery charging connectors with respect to SAE JI772 in the USA [41] and IEC 62196 in Europe [42].

Six-phase integrated battery chargers normally consist of a six-phase machine, inverter, and battery with DC-DC conversion stage, which is used to maintain the DC link voltage at a predefined level, e.g., 600 V, through boost operation [8, 16]. An asymmetrical six-phase ($\delta = 30^{\circ}$), symmetrical six-phase ($\delta = 60^{\circ}$), or dual three-phase ($\delta = 0^{\circ}$) layouts are possible winding topologies, where δ is the spatial phase shift between the two three-phase winding sets. The asymmetrical six-phase winding topology is the best candidate in the integrated EV charging applications since it minimizes the rotor loss index in the motoring mode [3] and considerably offers lower net radial forces in the charging compared to the dual three-phase layout [8].

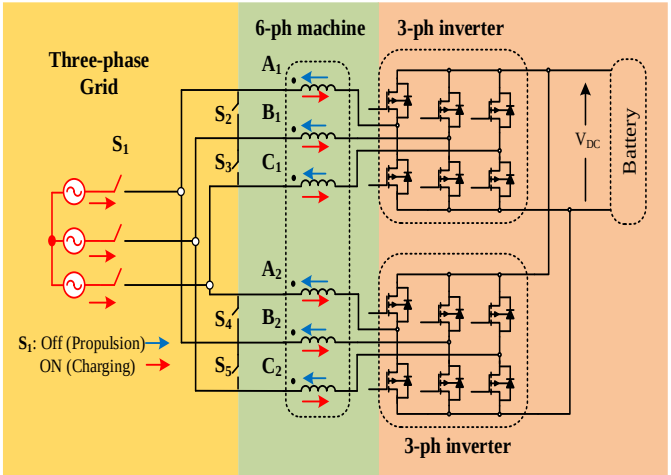

Fig. 1. Scheme of a six-phase integrated EV battery charger.

Therefore, the asymmetrical six-phase winding configuration is chosen in this analysis rather than the other winding layouts. The asymmetrical integrated OBC configuration is shown in Fig. 1 and can be reviewed in [8]. The operation under both the propulsion and charging has been elaborated as well.

From a control perspective, the reference charging current components are controlled such that the direct component is maximized, while the quadrature current component is set to nullified. As a result, Unity power factor operation at the grid side is ensured. The employed machine windings are used for grid current filtration [12, 13].

B. PM Machine Equipped with FSCW

Although the majority of existing EVs adopt distributed winding (DW) [11], FSCW arrangements have shown promise in recent studies. For example, the BMW i3 motor employs a DW with 72-slot/12-pole [43], while the FSCW with 0.5 slot/pole/phase is deployed in the stator of the Honda Insight [21]. The BMW i3 motor is an interior PM (IPM) and the Honda Insight utilizes an SPM machine. Fig. 2 shows the stator of the BMW i3 and Honda Insight, respectively.

FSCW layouts are more advantageous than their DW counterparts. These advantages include high copper fill factor, short end turns, low cogging torque, and improved flux-weakening capability [10, 44]. On the other hand, FSCW arrangements suffer from the distorted air gap flux distribution owing to high harmonic contents in the winding magnetomotive force (MMF). These sub and super space harmonics yield rotor core losses, rotor heating, and noise and vibrations in the mechanical structure [45]. Several work has been conducted in the literature to mitigate the above-mentioned drawbacks based on three-phase [46, 47] and multi-phase configurations [45, 48]. However, the employment of multi-phase machines entails a more complex converter and controller. The multi-objective optimization of FCSW-based PM machine has been recently elaborated to improve the torque density [46]. Moreover, several electromagnetic vibration sources have been investigated aiming at the design of PM machine with FSCW to decrease the electromagnetic vibration [47]. Furthermore, a unique multi-phase FSCW layout, i.e., 11-slot/10-pole, has been compared with the conventional 12-slot/10-pole [45]. As a result, critical radial forces are reduced in the new design based on the force compensation method.

Even though the adopted winding configuration has an impact on the performance of the integrated OBC, the performance of PM machine with FSCW under the EV charging process has not been comprehensively addressed in the available literature. An extensive review of multiphase FSCW slot/pole combinations, that can easily/practically be used as a viable powertrain for available EV designs, has been presented under both the propulsion and charging modes of operation [3]. This study addressed several factors regarding the selection of optimal slot/pole combinations including the winding factor and rotor loss index. However, peak-to-peak torque ripple, rotor losses, noise and vibration levels have not been considered. Therefore, various slot/pole combinations will be comprehensively addressed to cover these factors. The number of poles is preferably selected as $2p = S \pm 1$ or $2p = S \pm 2$ with regard to odd and even number of slots, respectively, where p is the number of pole pairs and is the S number of slots. That is why, six slot/pole combinations will be optimally designed; namely, 12-slot/10-pole, 12-slot/14pole, 24-slot/22-pole, 24-slot/26-pole, 36-slot/34-pole, and 36-slot/38-pole. The design optimization process of the selected slot/pole combination is elaborated in the following section.

III. Overview of Design Optimization Process

The design optimization process is introduced in this section. Firstly, the proposed machines are designed based on the MEC analytical model introduced in [32]. Table II reveals the machine design specifications, which are based the commercial BMW i3 motor [11]. Then multi-objective optimization strategy is discussed in detail. From EV's design perspective, several optimization objectives and constraints need to be carefully determined. This paper considers the machine overall cost and demagnetization risk, a notable contribution of this analysis. The employed asymmetrical six-phase SPM machines with various slot/pole combinations are presented in Fig. 3.

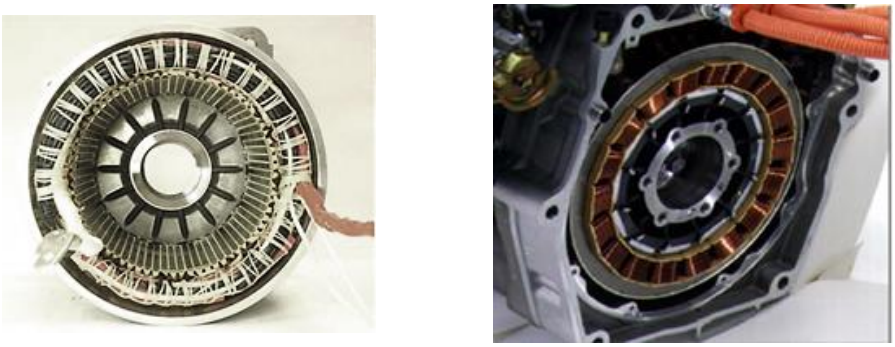

(a) (b)

Fig. 2. Stator windings. (a) BMW i3 [43], (b) Honda Insight [21].

Based on the machine design specifications listed in Table II, the proposed machines with several slot/pole combinations can initially be designed. To get a fair comparison, all motors are designed with the same air gap flux density, stator electrical loading, stack length to air gap diameter ratio, and slot fill factor. The initial geometrical dimensions are first defined based on the sizing equation [49]. Thereafter, the required output power and DC link voltage determine the rated RMS current and number of turns. Finally, the output efficiency and power density constitute the cost values for the Pareto front optimization technique. For example, the Pareto front between the efficiency and power density of the 12-slot/10-pole machine is depicted in Fig. 4. Accordingly, the initial machine is visualized. Moreover, all electromagnetic performances, including per-phase flux linkage, voltages, mean torque, and core losses, can be obtained on the basis of the parametric MEC model [32].

From an EV perspective, the output torque is the key performance target because it supports the EVs through high starting, frequent acceleration, and overload climbing. Therefore, it is maintained through the optimization process of the proposed six slot/pole combinations. Minimum peak-to-peak torque ripple and core losses, i.e. stator and rotor core losses, are crucial as well in both the motoring and charging modes of operation. The peak-to-peak torque ripple results in noise and vibration in PM machines, while the core losses may cause thermal demagnetization. Moreover, the six machines are compared considering the demagnetization capability and overall cost, i.e., rotor, stator, PMs, and copper costs.

Therefore, peak-to-peak torque ripple, core losses, and overall cost constitute the optimization objectives in the motoring mode. Meanwhile, torque ripple, core losses, and maximum magnetic field strength in magnets are the main optimization objectives during the charging process.

TABLE II. SPM machines design specifications.

BMW i3 requirements	
Rated power (kW)	125
Rated speed (rpm)	5000
Maximum speed (rpm)	10000
Rated torque (Nm)	240
Line current peak value (A)	156
DC link voltage (V)	600
Air gap flux density (T)	0.85
Stack length to air gap diameter ratio	0.7333
Stator electrical loading (A/mm)	15

The maximum magnetic field strength in magnets is used as an indicator of the demagnetization capability under charging and the ratio of the magnetic field strength to the magnet coercivity is defined as the demagnetization risk. The aforementioned objectives cannot be achieved concurrently. Therefore, the optimum trade-off among these objectives has been proposed. The optimization model aims at minimizing the objective function (1) with the variation in decision variables X_i such as magnet thickness (Y_m), tooth-tang depth (d_1), core back width (Y_{sb}), tooth width (W_t), slot opening ratio (t_{so}/τ_{so}), and PM width to pole pitch ratio (α_{PM}), as listed in Table III. The parametric model that highlights these design variables is shown in Fig. 5. Several constraints are adjusted to fairly compare between the optimized machines such as – the average developed torque (T_{mean}), the flux density in the tooth tips (B_{tooth}), and the current density (J).

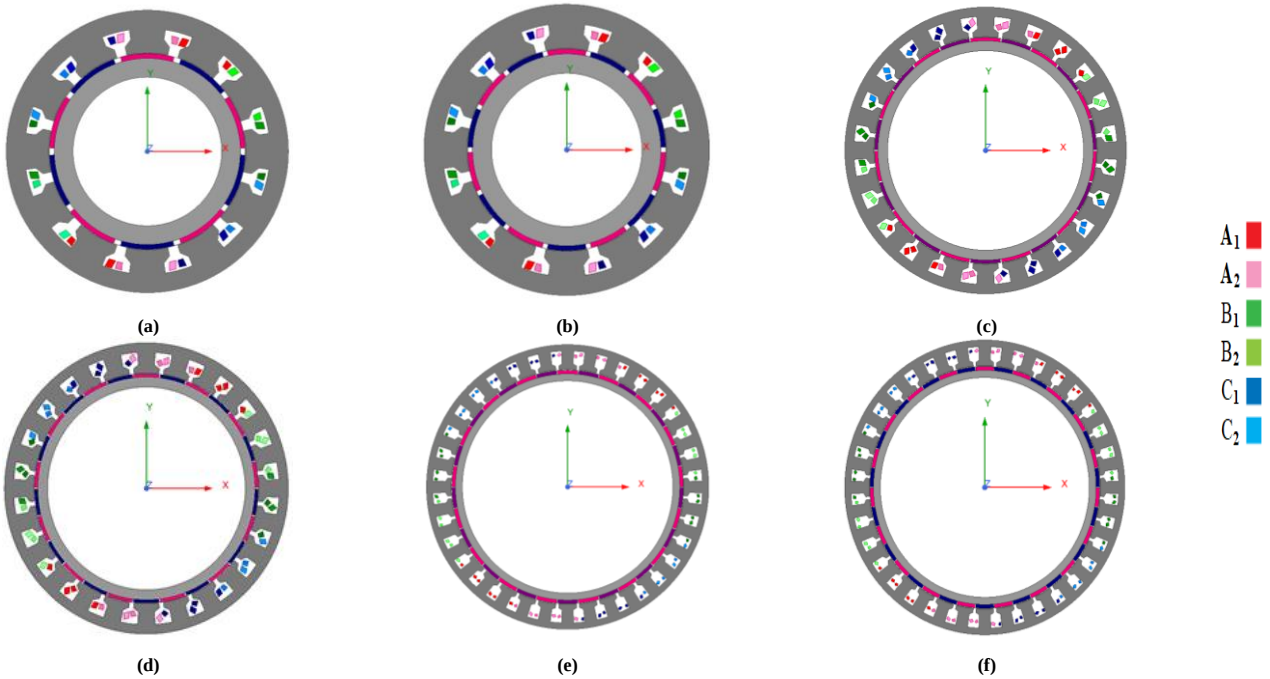

Fig. 3. 2D configuration of the proposed slot/pole combinations. (a) 12-slot/10-pole, (b) 12-slot/14-pole, (c) 24-slot/22-pole, (d) 24-slot/26-pole, (e) 36-slot/34-pole, (f) 36-slot/38-pole.

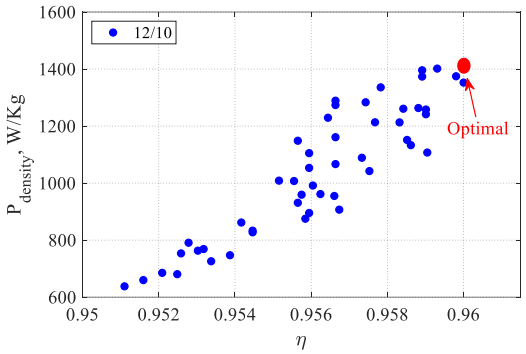

Fig. 4. Pareto front for 12-slot/10-pole machine.

The current density mainly depends on the cooling type, at which J (A/mm^2) is 2-4 when the convection air cooling is used; however, water stator jacket cooling improves the value of J to 6-14 [50]. Current, liquid cooling is utilized by Tesla and BMW [51]. Therefore, the current density is adjusted at 13 A/mm^2, as given by (2). The global optimization system can be composed as follows:

$$\min_{X_i} F(X_i) = \lambda_1 \frac{T_{ripple}^{prop}(X_i)}{T'^{prop}_{ripple}} + \lambda_2 \frac{P_{core}^{prop}(X_i)}{P'^{prop}_{core}} + \lambda_3 \frac{f_{cost}(X_i)}{f'_{cost}} + \lambda_4 \frac{H_{max}^{charg}(X_i)}{H'^{charg}_{max}} + \lambda_5 \frac{T_{ripple}^{charg}(X_i)}{T'^{charg}_{ripple}} + \lambda_6 \frac{P_{core}^{charg}(X_i)}{P'^{charg}_{core}} \quad (1)$$

where

$$\overrightarrow{X_i} = \left[Y_m, d_1, Y_{sb}, W_t, \frac{t_{so}}{\tau_{so}}, \alpha_{PM}\right]$$

$$\text{Subject to} \quad \begin{gathered} J \le 13\ A/mm^2 \\ B_{tooth} \le 1.7\ T \\ T_{mean} \ge 240\ Nm \\ T_{ripple} \le 8\ \% \\ X_i^{min} \le X_i \le X_i^{max} \end{gathered} \quad (2)$$

where $T_{ripple}^{prop}(X_i)$, $P_{core}^{prop}(X_i)$, $f_{cost}(X_i)$, $H_{max}^{charg}(X_i)$, $T_{ripple}^{charg}(X_i)$, and $P_{core}^{charg}(X_i)$ are the values of torque ripple under propulsion, core losses under propulsion, machine overall cost, maximum magnetic field strength under charging, torque ripple under charging, and core losses under charging, respectively. Meanwhile, the corresponding initial values are T'^{prop}_{ripple}, T'^{prop}_{core}, f'_{cost}, H'^{charg}_{max}, T'^{charg}_{ripple}, and P'^{charg}_{core}, respectively. Moreover, λ_1, λ_2, λ_3, λ_4, λ_5, and λ_6 are the weight factors of the six optimization objectives, respectively, whereas $\lambda_1 + \lambda_2 + \lambda_3 + \lambda_4 + \lambda_5 + \lambda_6 = 1$. In that case, the same weighting factor is used for the six objectives due to the equal importance of them.

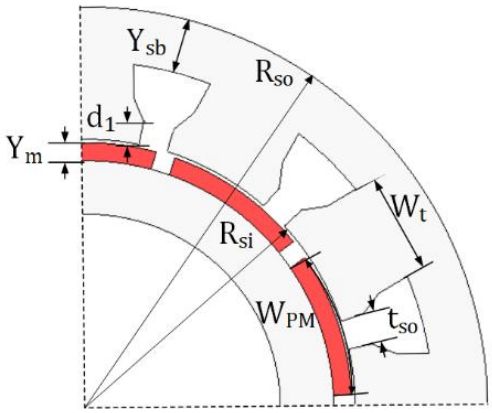

Fig. 5. Parametric model of the SPM machine.

This paper presents a multi-objective optimization approach based on a MOGA optimization [52] to define optimum designs. Accordingly, global sensitivity analysis is utilized to determine the effect of each design parameter on the various optimization objectives [53]. In this paper, sensitivity analysis indices based on functional decomposition of variance $H(X_i)$ and comprehensive sensitivity index $G(X_i)$ are obtained by (3) and (4), respectively:

$$H(X_i) = \frac{Var[E(Y/X_i)]}{Var(Y)} \quad (3)$$

$$G(X_i) = \lambda_1 |H_{ripple}^{prop}(X_i)| + \lambda_2 |H_{core}^{prop}(X_i)| + \lambda_3 |H_{cost}(X_i)| + \lambda_4 |H_{demag}^{charg}(X_i)| + \lambda_5 |H_{ripple}^{charg}(X_i)| + \lambda_6 |H_{core}^{charg}(X_i)| \quad (4)$$

where Y and X_i are the optimization output and design parameters, respectively. $E(Y/X_i)$ represents the average value of Y when X_i is constant. $Var[E(Y/X_i)]$ and $Var(Y)$ are the variances of $E(Y/X_i)$ and Y, respectively. The sensitivity indices that corresponds to the torque ripple under propulsion, core losses under propulsion, machine overall cost, maximum magnetic field strength under charging, torque ripple under charging, and core losses under charging are $H_{ripple}^{prop}(X_i)$, $H_{core}^{prop}(X_i)$, $H_{cost}(X_i)$, H_{demag}^{charg}, $H_{ripple}^{charg}(X_i)$, and $H_{core}^{charg}(X_i)$, respectively. As a result, the selected design variables are classified into high-sensitive (HSP) and low-sensitive (LSP) parameters.

Moreover, the Response surface (RS) methodology shows how the optimization objectives vary with respect to the variation in key design variables [54]. Consequently, the variation range of HSP is enhanced resulting in notable decrease in the computational burden of the following MOGA-based optimization. In this paper, Box–Behnken designs for RS methodology were developed with only 15 sampling points of the three high-sensitive variables.

TABLE III. Design parameters variation range.

Parameter	12/10	12/14	24/22	24/26	36/34	36/38
Y_m (mm)	[4.5,7.5]					
d_1 (mm)	[7,9.5]		[4,6]		[3,5]	
Y_{sb} (mm)	[18,26]		[9.5,13.5]		[5,8]	
W_t (mm)	[38,48]		[17,23]		[36,44]	
t_{so}/τ_{so}	[0.15,0.3]					
α_{PM}	[0.7,0.95]					

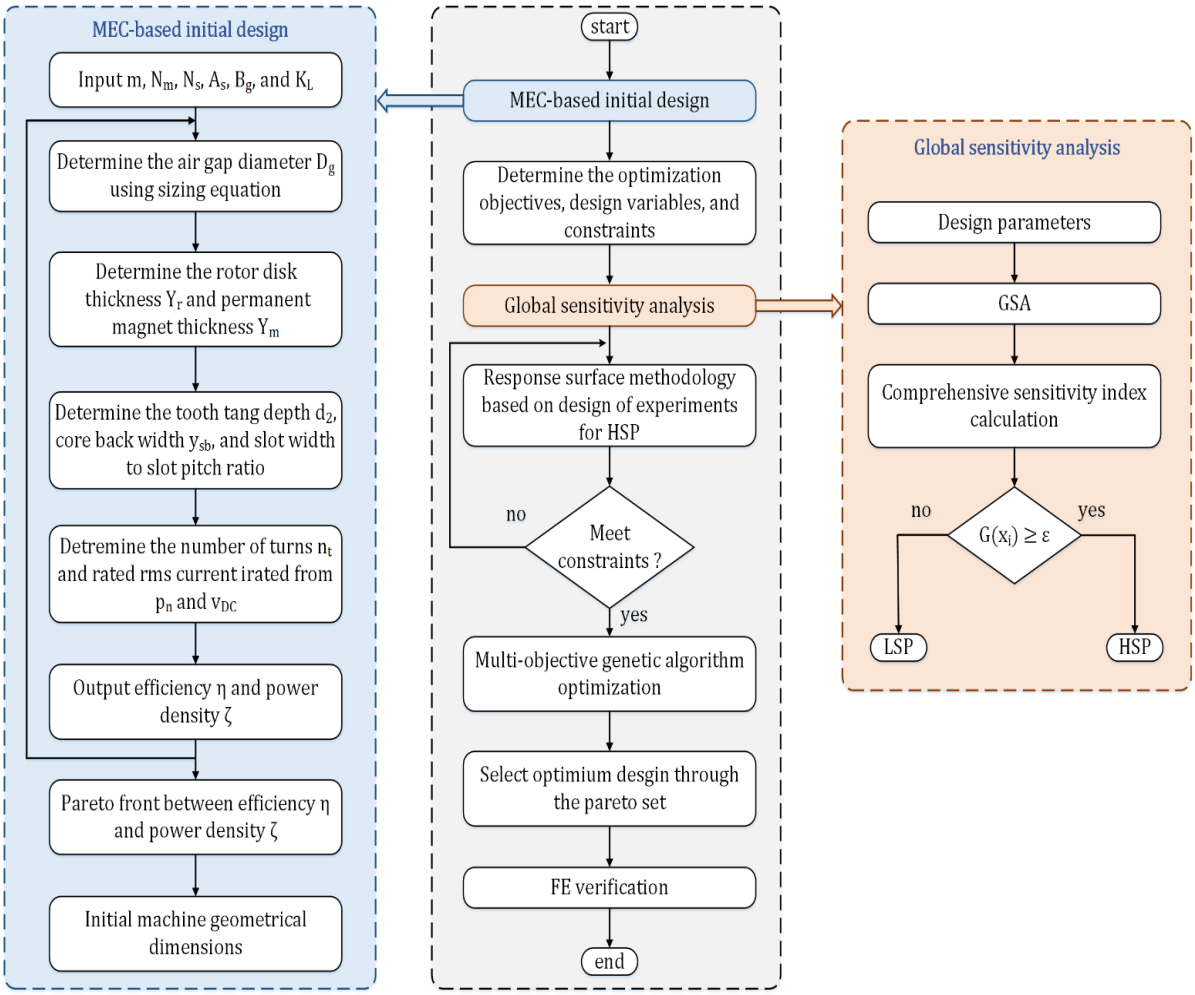

Fig. 6. Flowchart of the design and multi-objective optimization process.

For clear presentation, the flow chart of the overall design optimization process of the asymmetrical six-phase SPM machines is shown in Fig. 6, which includes several steps as follows:

- Initial machine design is obtained based on the efficient MEC model, as described in the previous subsection.
- Optimization objectives of torque ripple, core losses, overall cost, and demagnetization capability are defined considering the EV's requirements. Moreover, the design variables and boundary constraints are determined.
- Sensitivity analysis technique is used to categorize the design variables into HSP and LSP parameters according to comprehensive sensitivity index $G(X_i)$ [55].
- RS technique has been utilized to enhance the optimization efficiency by illustrating the variation in optimization objectives with respect to the design variables. Consequently, the RS methodology has been adopted in this study to improve the variation range of HSP and decrease the computational burden.
- MOGA-based optimization is used to define the optimum trade-off among the six-objectives; accordingly optimal design point is determined.
- Electromagnetic performances of the optimal machines are validated using finite element simulations.

As an illustrative example, the optimization results of the 12-slot/10-pole under both operational modes are shown in Fig. 7. The optimized machine parameters are listed in Table IV. The electromagnetic performances of the selected six slot/pole combinations are discussed and compared in the following section.

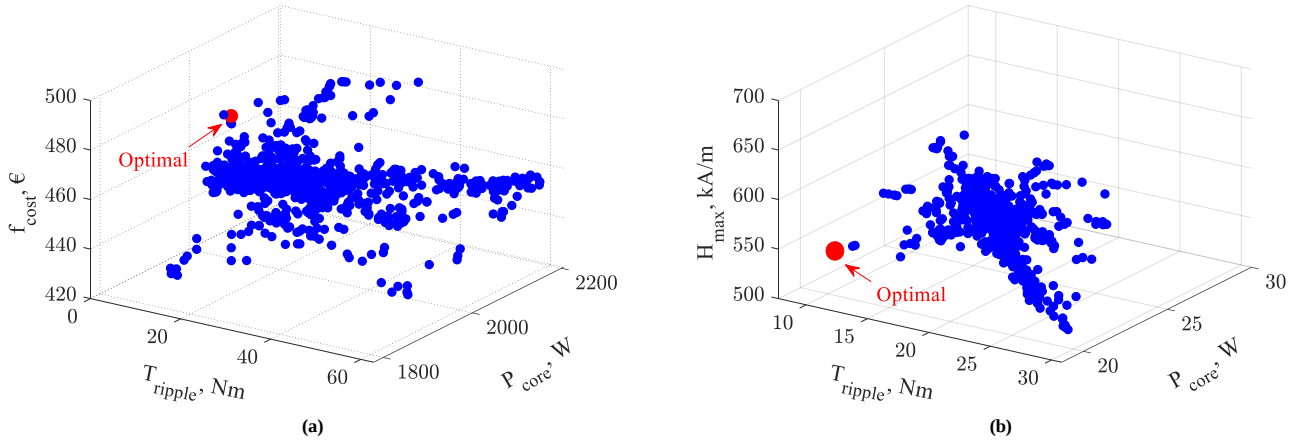

(a) (b)

Fig. 7. Optimization results of the 12-slot/10-pole machine. (a) in the propulsion. (b) in the charging.

TABLE IV. SPM machine parameters.

Parameter	Symbol	12/10	12/14	24/22	24/26	36/34	36/38
Stator outer diameter (mm)	D_{so}	343	329.2	302.8	298.4	289.2	286.8
Stator inner diameter (mm)	D_{si}	255.2	255.2	253.6	253.6	253.4	253.4
Stack length (mm)	L_{eff}	187.1	187.1	186	186	185.8	185.8
Air gap length (mm)	g	1.4	1.4	1.4	1.4	1.4	1.4
Depth of stator slot (mm)	d_{ss}	19.8	19.6	13.8	13.3	10.9	10.4
Slot-opening width (mm)	t_{so}	10.6	10.6	5.1	5.1	3.4	3.4
Rotor outer diameter (mm)	D_{ro}	252.4	252.4	250.8	250.8	250.6	250.6
Shaft diameter (mm)	D_{shaft}	192.4	206	218.2	221	223.6	224.2
Rotor disc thickness (mm)	Y_r	25.6	18.7	11.7	10.1	8.1	7.5
Magnet thickness (mm)	Y_m	5.8	6	5.6	6.1	7.3	6.8
Gap between magnets (mm)	d_{pm}	11.6	17.6	4.1	2.6	2.3	2.6
Magnet volume (mm^3)	V_{pm}	71388	49012	32977	36587	27946	22841
No. of turns per coil	N_t	5	4	2	2	1	1
rated rms current (A)	I_a	110.3	135	133	132.7	175.6	175.2
Phase resistance (Ω)	$\mathcal{R}$	0.0068	0.0044	0.0044	0.0044	0.0025	0.0025

IV. ELECTROMAGNETIC PERFORMANCES

In this section, the optimal machines are broadly compared with respect to torque performances, core losses, net radial forces, overall cost, and more importantly demagnetization capability. The winding factor (k_w), greatest common divisor, lowest common multiple, and the rotor index (R_i) have been previously introduced in [3]. Moreover, FE simulations are conducted to validate the proposed design optimization process. For FSCW-based PM machines, the torque-producing component normally is located at the number of pole pairs (p) which is accompanied by the inevitable slot harmonic. The higher the winding factor, the better the torque density. However, the torque-producing component should be nullified under charging to ensure zero average torque production, a key demand of the integrated EV charging applications. Fig. 8 shows the torque profiles of the six motors in the charging process. Although zero average torque production is ensured by the selected slot/pole combinations, the peak-to-peak torque ripple is slightly reduced at higher slot/pole combinations (e.g. the torque ripple is 8.37 Nm for the 36-slot/34-pole machine compared to 10.87 Nm when the 12-slot/10-pole machine is employed).

For the sake of comparison, the average developed torque is maintained in the propulsion mode of operation. The torque characteristics and profiles under propulsion are depicted in Figs. 9 and 10, respectively. From Fig. 9, the rated current varies for the six machines to adjust the average torque production at a predefined level. This is mainly because of the variation in the power factor.

Despite the fact that the six selected slot/pole combinations develop almost the same average torque under propulsion, the torque ripple, the main cause of vibration and noise in PM machines, is substantially decreased when higher slot/pole combinations are employed. For example, the torque ripple value reaches 2.70 Nm for the 36-slot/38-pole machine compared to 3.12 and 8.36 Nm for the 24-slot/26-pole and 12-slot/14-pole machines, respective, as shown in Fig. 10. In order to verify the results obtained from the MEC model, Torque and voltage profiles of the 12-slot/10-pole machine under both operational modes are given in Fig. 11 and 12, respectively.

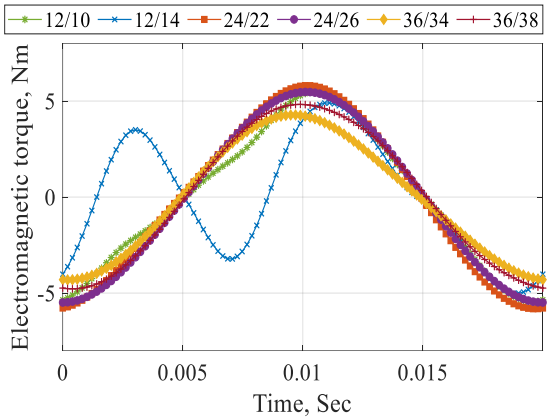

Fig. 8. Electromagnetic torque under charging.

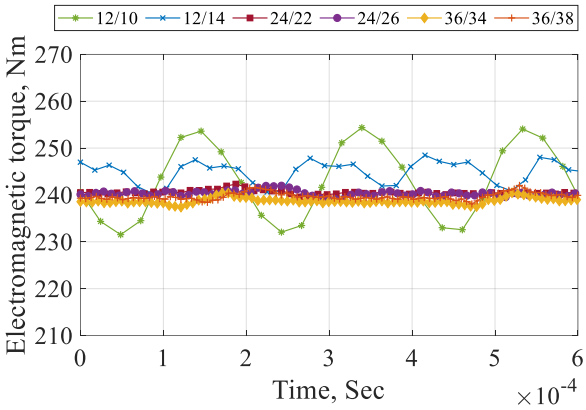

Fig. 10. Electromagnetic torque under propulsion.

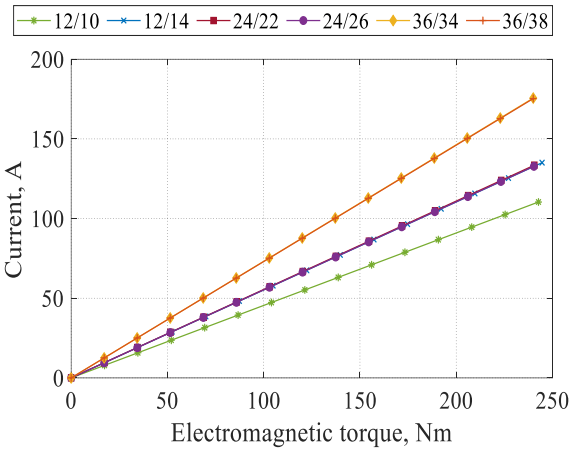

Fig. 9. Torque characteristics.

Furthermore, the PM eddy current loss is estimated under both operational modes using the ANSYS Electronics Desktop. Fig. 13 depicts the iron losses under both the propulsion and charging modes, including the copper loss, stator and rotor core losses, and PM eddy current loss. It can be noted that the PM eddy current loss is estimated at a speed of 1000 rpm. The copper loss is the same for all slot/pole combinations because the same stator electrical loading is applied. Moreover, the charging mode is initiated at the same propulsion current; therefore, the copper loss has not been added under charging to avoid repetition. The stator and rotor core losses are considerably increased under propulsion due to the increase in the frequency. The same conclusion cannot be drawn under charging, at which the core losses are decreased at higher slot/pole combinations. Similarly, the PM eddy current loss is expected to be increased with the increase in frequency; however, the PM eddy current loss is considerably reduced at higher slot pole combination due to the reduction in the PM volume.

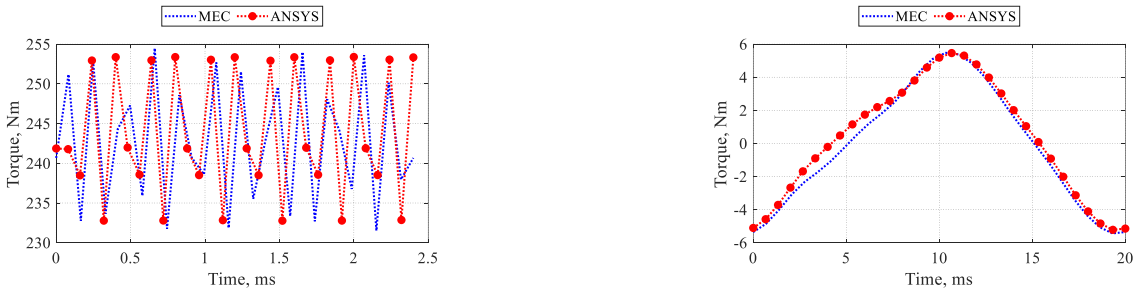

Fig. 11. Torque profiles of the 12-slot/10-pole machine. (a) in the propulsion. (b) in the charging.

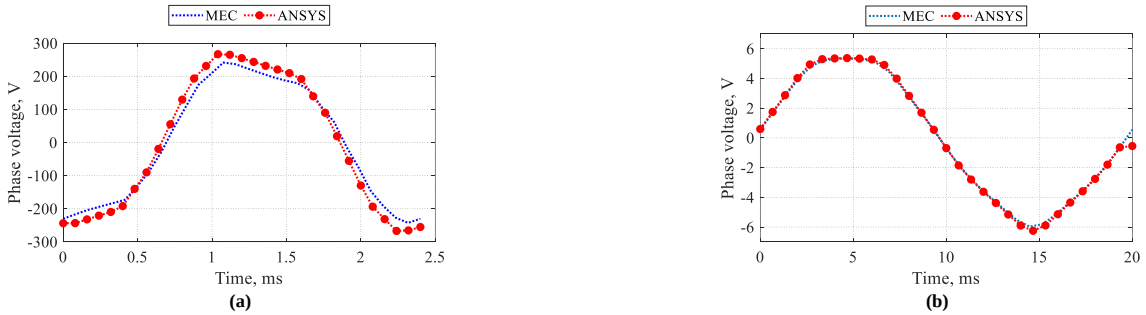

Fig. 12. Phase voltage profiles of the 12-slot/10-pole machine. (a) in the propulsion. (b) in the charging.

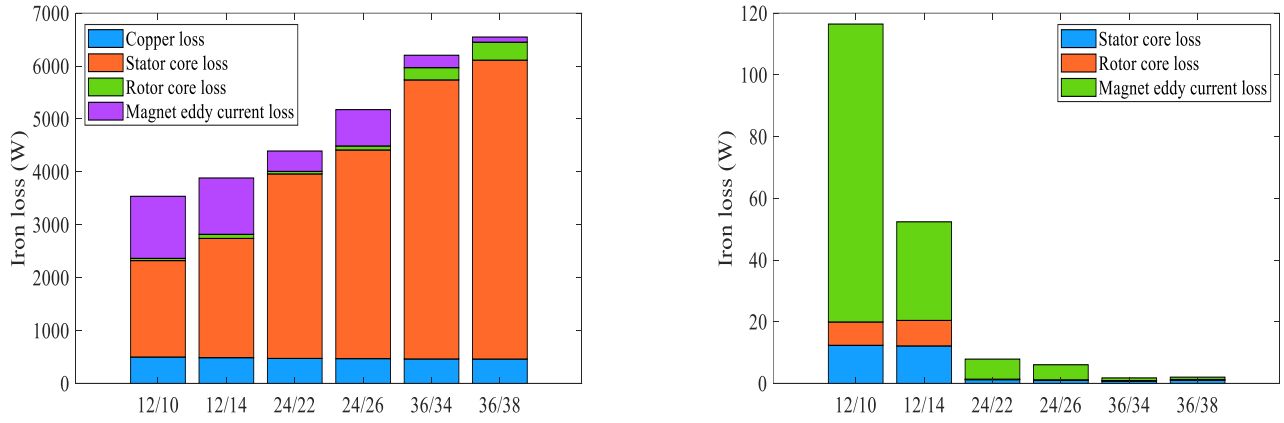

Fig. 13. Iron losses under both operational modes. (a) Propulsion. (b) Charging.

Another key factor in selecting an optimal machine is the unbalanced magnetic pull (UMP) since it affects the performance and service life of the PM machines. The relation between the electromagnetic forces and air-gap flux densities is expressed using Maxwell Stress Tensor method [56]. The radial F_r and circumferential F_θ force components are first calculated by the radial B_r and circumferential B_θ flux densities, as follows:

$$F_r = \frac{1}{\mu_o}\frac{B_r^2 - B_\theta^2}{2}, \quad F_\theta = \frac{1}{\mu_o} B_r B_\theta, \tag{5}$$

where μ_o is the vacuum permeability. Then, the x and y components of the UMP are deduced from F_r and F_θ force components, which is expressed as follows:

$$\begin{aligned} F_x &= \int_0^{L_{eff}} \int_0^{2\pi R_g} (\mathrm{F_r}\cos(\theta_\mathrm{m}) - \mathrm{F_\theta}\sin(\theta_\mathrm{m}))\mathrm{d}\theta\mathrm{d}z, \\ F_y &= \int_0^{L_{eff}} \int_0^{2\pi R_g} (\mathrm{F_r}\sin(\theta_\mathrm{m}) + \mathrm{F_\theta}\cos(\theta_\mathrm{m}))\mathrm{d}\theta\mathrm{d}z, \end{aligned} \tag{6}$$

where, R_g is the enclosed surface in the average air gap radius and θ_m is the circumferential angle. The force computations under charging for the six motors are shown in Fig. 14. The comparison shows that the higher the slot/pole combination, the higher radial forces; however, the forces are low up to 26 N due to the adoption of the asymmetrical winding topology. form force perspective, this indicates the validity of the elected slot/pole combinations.

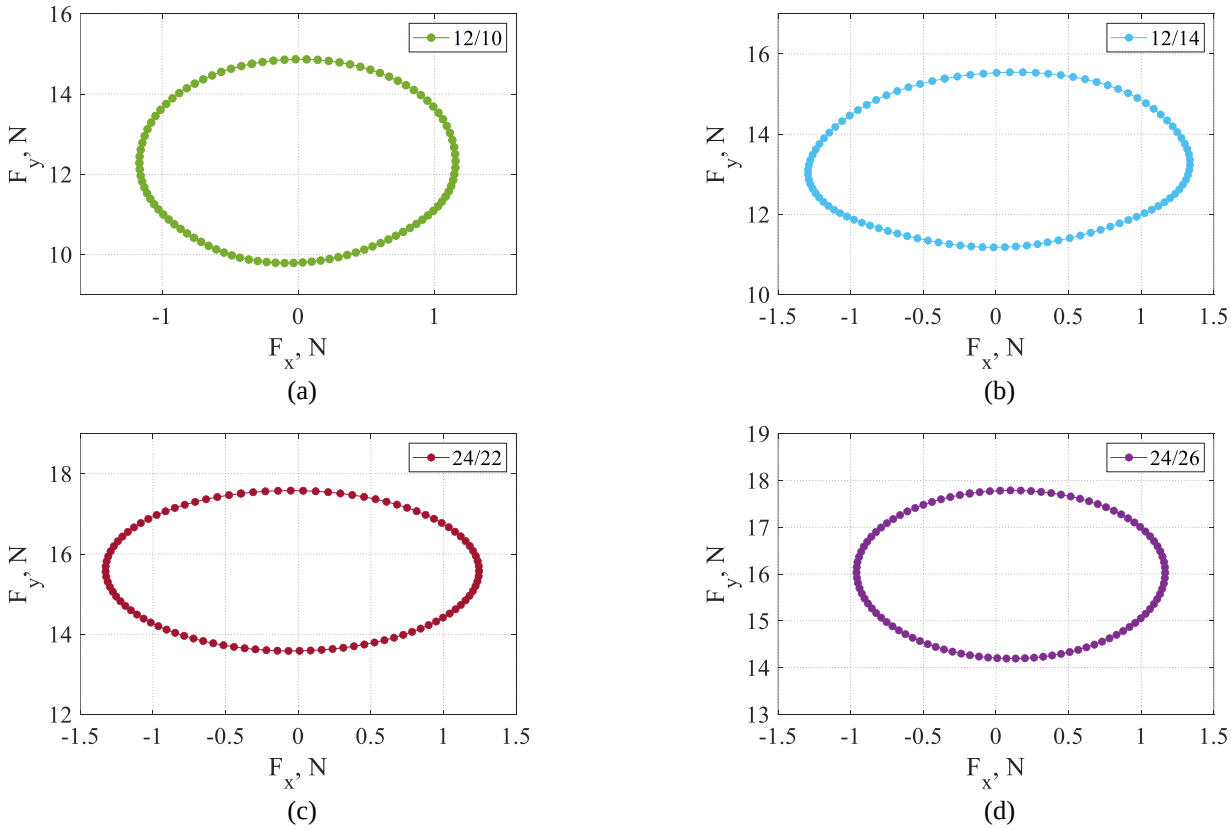

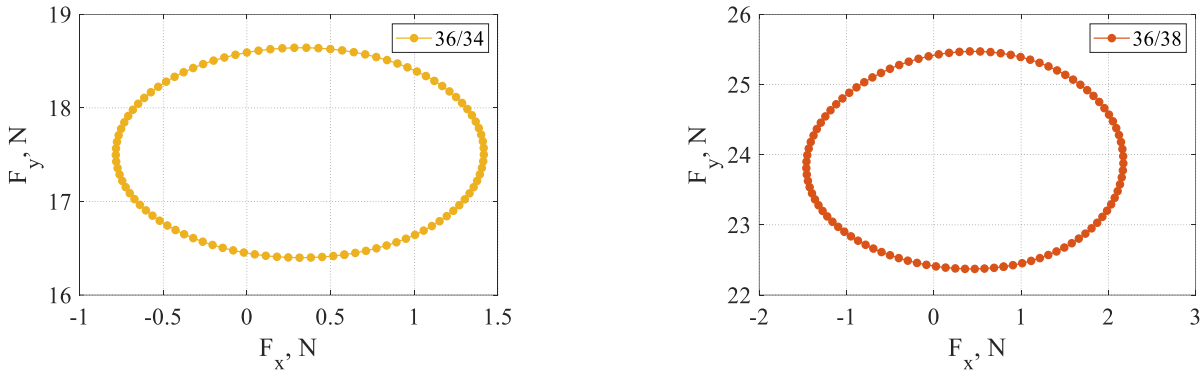

(e) (f)

Fig. 14. x-y electromagnetic forces on the rotor in the charging mode.

Moreover, the PM demagnetization may occur due to the flow of currents in the stator windings under charging. Thus, the PM machine performance deteriorates. Therefore, this study determines the demagnetization risk by checking the maximum magnetic field strength, a notable contribution of this study. Arnold N40SH type of NdFeB rare-earth magnet is utilized in this study, at which the demagnetization occurs at 891 kA/m at a temperature of 100° and at 444 kA/m at a temperature of 150°. Fig. 15 presents the magnetic field intensity distribution of various slot/pole combinations in the charging process. Clearly, the maximum magnetic field intensity is 545 kA/m for the 12-slot/10-pole machine, which is less than the coercivity. It can be noted that the temperature has a clear impact on PM demagnetization [57]. The demagnetization risk is used to evaluate the demagnetization capability of the employed slot/pole combinations and is defined as follows:

$$demag\_risk = \frac{H_{max}^{charg}}{H_c} \times 100 \qquad (7)$$

Where $demag\_risk$ is the demagnetization risk and H_c is the coercivity of the N40SH PM. Demagnetization of the six motors is assessed at the temperatures of 100° and 150°, as listed in Table V. Consequently, the demagnetization risk is considerably reduced at high slot/pole combination, e.g., the risk is 61.2, 46.7, and 42.1 when 12-slot/10-pole, 24-slot/22-pole, and 36-slot/34-pole machines are employed at the temperature of 100°, respectively.

TABLE V. Demagnetization capability of the motors.

Demagnetization risk (%)	12/10	12/14	24/22	24/26	36/34	**36/38**
@ 100° *c*	61.2	58.0	46.7	50.4	42.1	41.2
@ 150° *c*	122.8	116.5	93.7	101.2	84.5	82.6

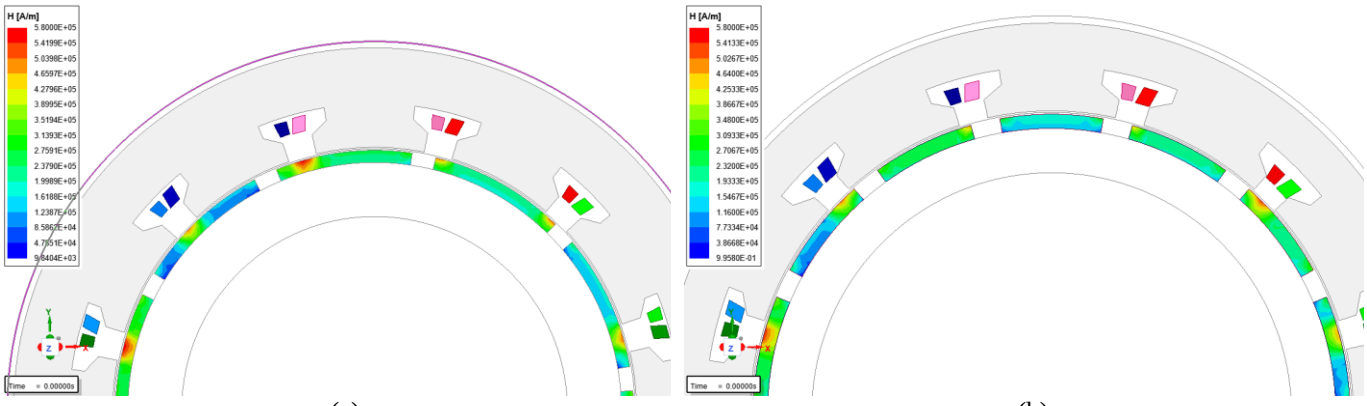

(a) (b)

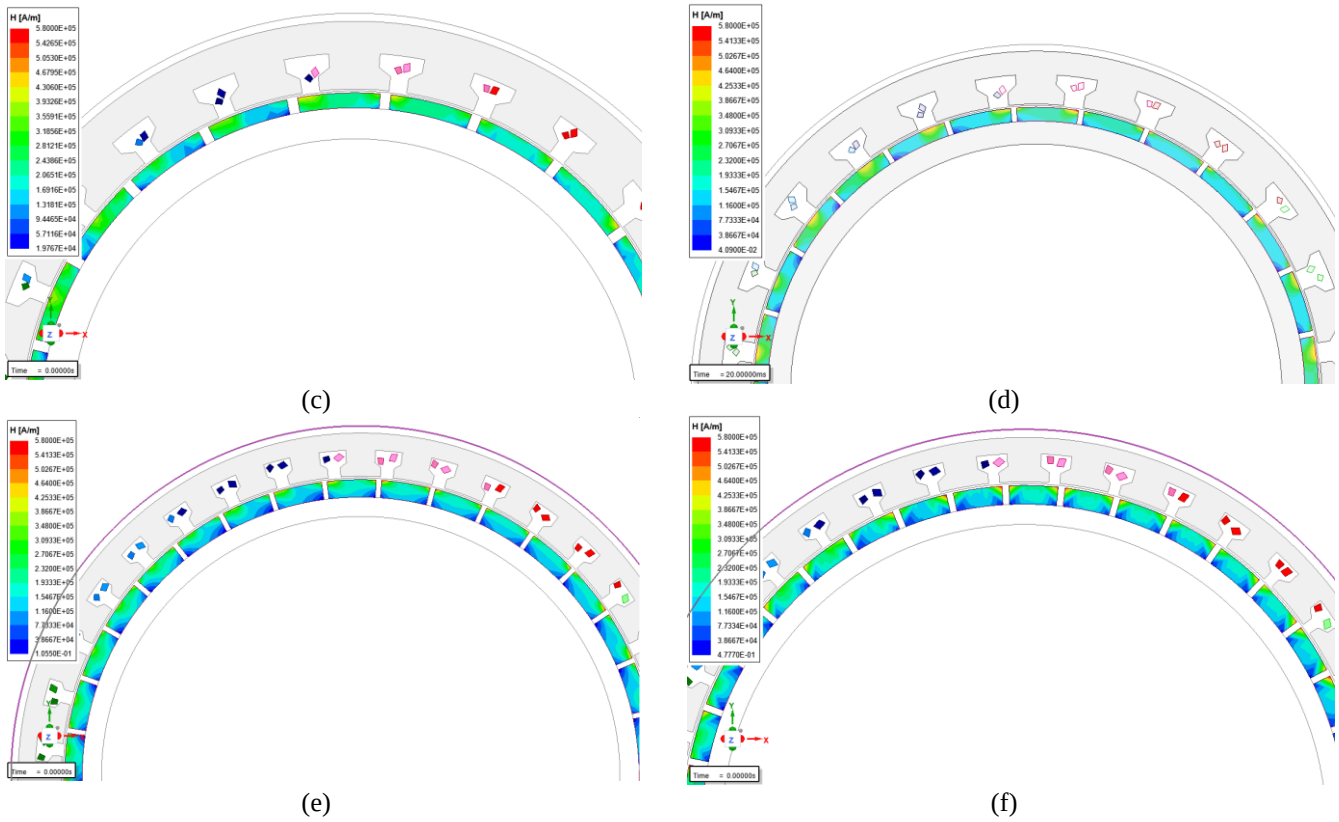

Fig. 15. Magnetic field intensity distribution of various slot/pole combinations under charging. (a) 12-slot/10-pole, (b) 12-slot/14-pole, (c) 24-slot/22 pole, (d) 24-slot/26-pole, (e) 36-slot/34-pole, (f) 36-slot/38-pole.

Moreover, the overall cost of the machines is predicted by the following equation [58]:

$$f_{cost} = C_{iron} \times (M_s + M_r) + C_{PM} \times M_{PM} + C_{copper} \times M_{coil} \quad (8)$$

where M_s, M_r, M_{PM}, and M_{coil} are the stator, rotor, PM, and coil masses, respectively. While C_{iron}, C_{PM}, and C_{copper} are their corresponding costs per kilogram. Table VI reveals the assigned materials and their costs per kilogram. the total mass is inversely proportional to the number of pole pairs. The machine overall cost is, therefore, reduced at higher slot/pole combinations, as proved in Table VII.

TABLE VI. Assigned materials and their costs per kilogram.

Machine part	Material	Cost per Kilogram (€/kg)
Coil	Copper	15
Stator core	M235-35A	3
Rotor core	M235-35A	3
Rotor magnet	N40SH	40

Finally, the efficiency maps of the six machines are calculated using ANSYS Electronics Desktop, as shown in Fig. 16. As expected, the 12-slot/10-pole machine offers the highest efficiency over other slot/pole combinations due to the considerable increase in the core losses.

Table VII presents a broad comparison between the six slot/pole combinations that accommodate asymmetrical six-phase configurations, shedding light on motoring performances, namely peak-to-peak torque ripple and core losses, as well as torque ripple, core losses, and demagnetization capability under charging. The given table also includes the machine overall cost as well as the power density. As is clear from Table VII, the following conclusions may be drawn:

- The torque ripple generally decreases as the slot/pole combination increases, e.g. the torque ripple is 22.91 and 2.70 Nm for the 12-slot/10-pole and 36-slot/38-pole machines, respectively.
- The frequency is increasing with higher number of poles. Thus, A steady but significant rise in the propulsion core losses is noted.
- The torque ripple is slightly reduced in the charging mode; however, a substantial reduction in the core losses can be seen with the higher slot/pole combination in the charging.
- The higher the slot/pole combination, the lower the maximum magnetic field strength; therefore, the lower demagnetization risk under charging.
- When the number of poles is increased, the total mass is decreased. Thus, the overall cost is reduced, e.g., the overall cost is 495.55 and 350.52 € for the 12-slot/10-pole and 36-slot/38-pole machines, respectively.
- The power density is substantially increased with higher number of rotor poles. This is mainly because the machine mass is considerably reduced with the increase in the machine rotor poles.

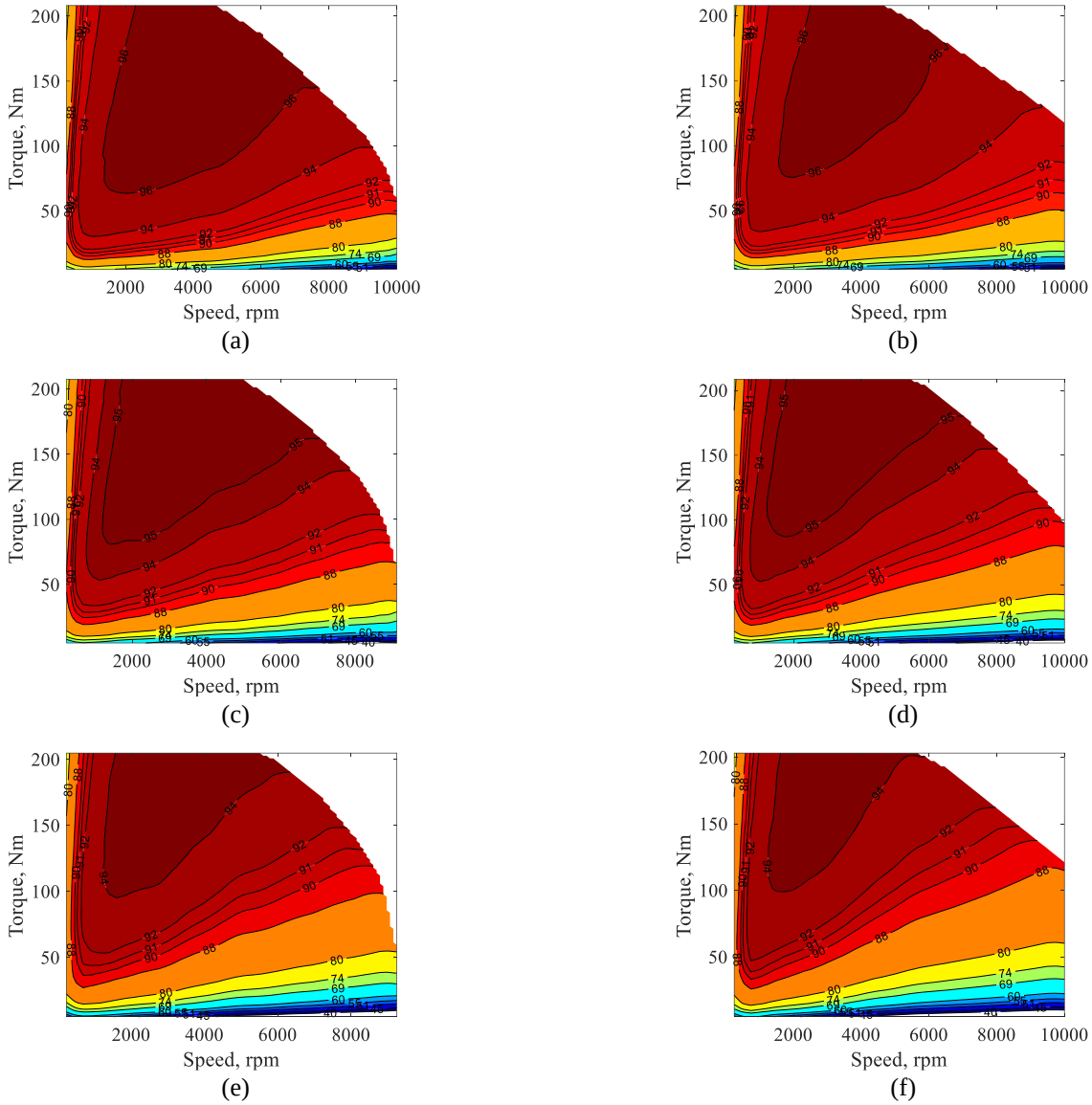

Fig. 16. Torque Efficiency maps of the proposed machines. (a) 12-slot/10-pole, (b) 12-slot/14-pole, (c) 24-slot/22 pole, (d) 24-slot/26-pole, (e) 36-slot/34-pole, (f) 36-slot/38-pole.

TABLE VII. Comparison of MEC and FE models.

Output	12/10		12/14		24/22		24/26		36/34		36/38	
	ANSYS	MEC	ANSYS	MEC	ANSYS	MEC	ANSYS	MEC	ANSYS	MEC	ANSYS	MEC
$T_{mean}^{prop}(Nm)$	243.9	242.5	245.2	244.4	240	240.5	240	240.2	240	240.1	240.52	240.67
$T_{ripple}^{prop}(Nm)$	20.6	22.91	6.23	7.74	1.97	2.86	2.74	3.12	2.65	2.92	2.44	2.70
$P_{core}^{prop}(W)$	1758	1862	2123	2326	3479	3536	3913	4012	5324	5487	5905	5965
$f_{cost}(€)$	495.55		426.50		359.35		363.58		388.08		350.52	
$H_{max}^{charg}(kA/m)$	552.3	545.35	495.23	517.04	408.54	416.13	480	449.28	393	375.20	382.1	366.96
$T_{ripple}^{charg}(Nm)$	10.68	10.87	9.74	9.83	11.54	11.63	10.89	10.95	7.04	8.37	9.3	9.90
$P_{core}^{charg}(W)$	23.77	19.93	23.27	20.44	1.7	1.39	1.39	1.16	1.43	0.94	1.89	1.34
$P_{density}(W/K_g)$	1422		1859		2762		3089		3661		3977	

V. EXPERIMENTAL VERIFICATION

To validate the effectiveness of the proposed design optimization process, an asymmetrical 2 kW 12-slot/10-pole SPM machine is constructed, and the experimental results are carried out on the test bench depicted in Fig. 17. The prototype machine design parameters are listed in Table VIII, while the assigned materials are revealed in Table VI. Both experimental and FE simulations are conducted at the rated speed of 1200 rpm, rated rms current of 3.2 A, and the DC-link voltage of 300 V. The conventional field-oriented control (FOC) is utilized in the motoring mode [59]. Whereas, the charging control structure, extensively explained in [60], is based on the conventional proportional-resonant (PR) controllers, as given in Fig. 18. The PR-based controller comprises several steps, as follows:

- Step 1: the grid current components are controlled such that the reference direct component, i_d^*, is maximized to ensure the maximum level of charging, while the quadrature component, i_q^*, is nullified to guarantee unity power factor operation at the grid side. Based on the reference grid current components, the reference sequence current components are determined.
- Step 2: the stator xy reference currents, i_{xy}^*, are controlled to the same value of the reference $\alpha\beta$ grid currents, $i_g^{\alpha\beta *}$, which are derived using the inverse Park's transformation. The grid is synchronized with the inverter through a phase-locked loop.
- Step 3: both the stator $\alpha\beta$ currents, $i_{\alpha\beta}$, and zero sequence current components, $i_{0^+0^-}$, are set to zero. Therefore, zero average torque production is ensured.
- Step 4: two PR-based current controllers are used to adjust $\alpha\beta$ and xy subspaces, while the zero-sequence subspace is controlled by only one PR controller, since $i_{0^+} = -i_{0^-}$.
- Step 5: the phase voltage components are obtained from the PR output voltage components using the inverse space decomposition (VSD) matrix [60]. Finally, the six-phase inverter currents are derived using sinusoidal pulse width modulation (SPWM).

TABLE VIII. SPM prototype machines design parameters.

Parameter	Symbol	Value
Stator outer diameter (mm)	D_{so}	177.6
Stator inner diameter (mm)	D_{si}	110.2
Stack length (mm)	L_{eff}	66.7
Air gap length (mm)	g	1
core back width (mm)	Y_{sb}	9.5
Rotor outer diameter (mm)	D_{ro}	108.2
Magnet thickness (mm)	Y_m	4.4
No. of turns per coil	N_t	73

(a)

(b)

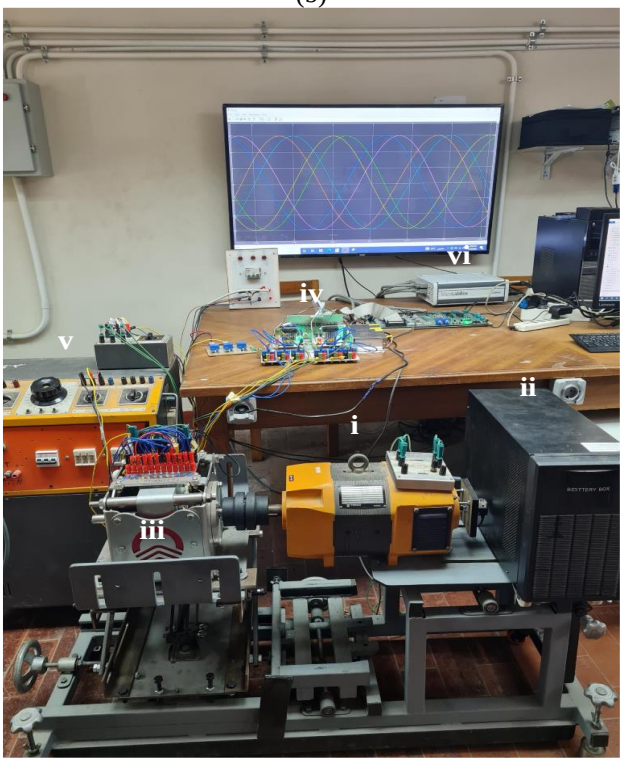

(c)

Fig. 17. Prototype SPM machine. (a) Stator. (b) Rotor. (c) test bench: (i) DC machine, (ii) battery box, (iii) six-phase 12/10 SPM machine, (iv) six-phase inverter, (v) three-phase grid, and (vi) driving controller.

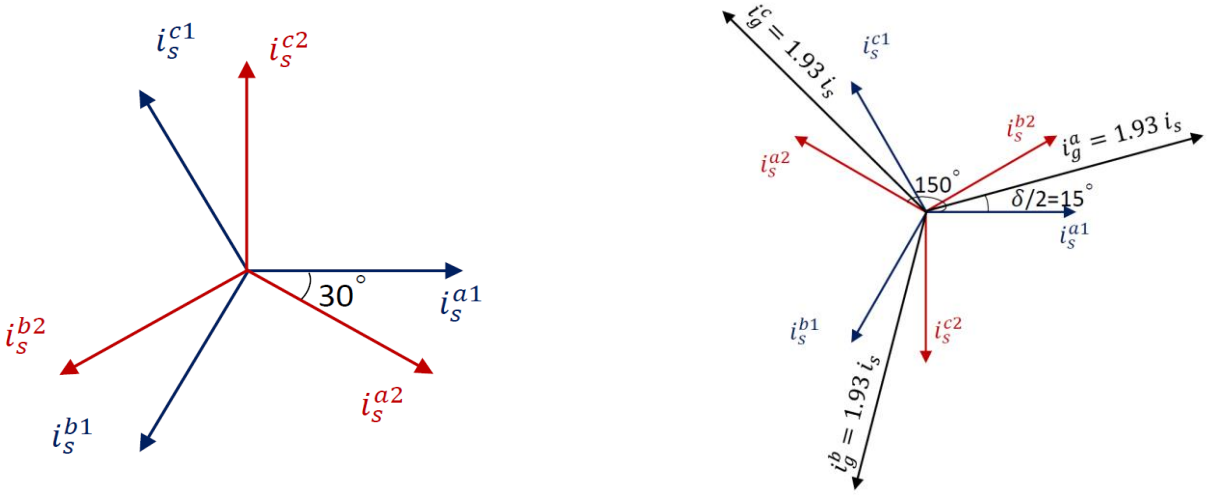

(a) (b)

Fig. 19. Asymmetrical six-phase phasor diagram. (a) Propulsion. (b) Charging.

A dSPACE 1202 model is utilized to perform the whole control strategy. Fig. 19 shows the asymmetrical six-phase phasor diagram in the propulsion ($\delta = 30^{\circ}$) and charging ($\delta = 210^{\circ}$) modes of operation, respectively. The experimental results under both the propulsion and charging modes of operation are presented in the following subsections.

A. Propulsion mode of operation

In the propulsion mode, the no-load back electromagnetic force (EMF) is presented in Fig. 20. It is clear that the back EMF from experiments and FE analysis show good agreement, with a slight increase in the amplitude of the experimental results. Moreover, Fig. 21 compares the average torque production between experiments and FE analysis at the rated current. It can be seen that the experimental average torque production is almost 16.1 Nm compared to 16.23 Nm obtained from the FE study. However, it was not possible to accurately measure the torque ripple magnitude with the limited frequency response of the employed torque sensor. Fig. 22 depicts the corresponding six-phase stator currents in the propulsion. Figs. 23 and 24 show the dynamic response of the prototype machine during propulsion mode. It is clear that the employed controller can efficiently respond to the speed change from 0 to 1000 rpm.

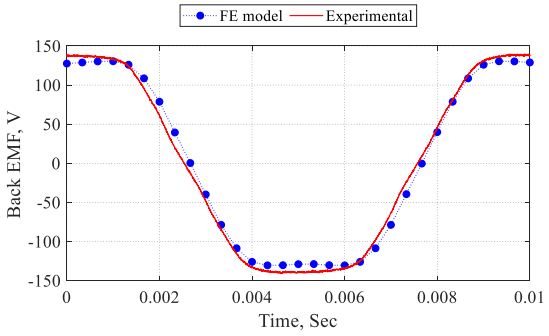

Fig. 20. Measured back EMF.

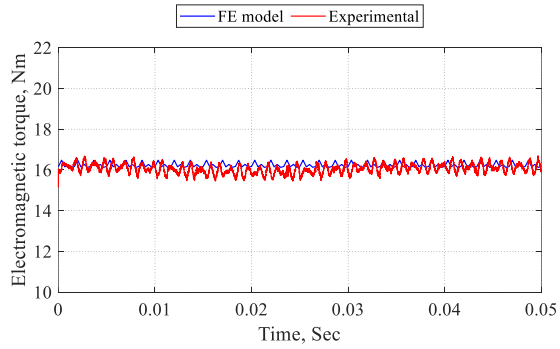

Fig. 21. Electromagnetic torque under propulsion.

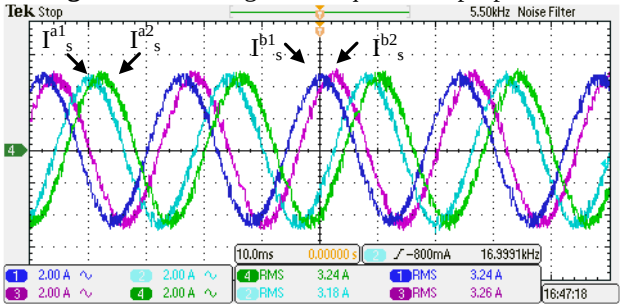

Fig. 22. Stator currents under propulsion.

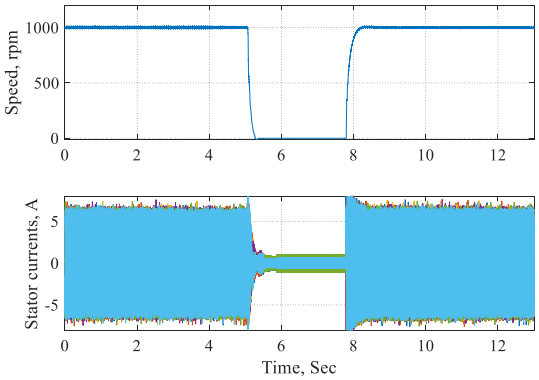

Fig. 23. Step speed response of the prototype machine.

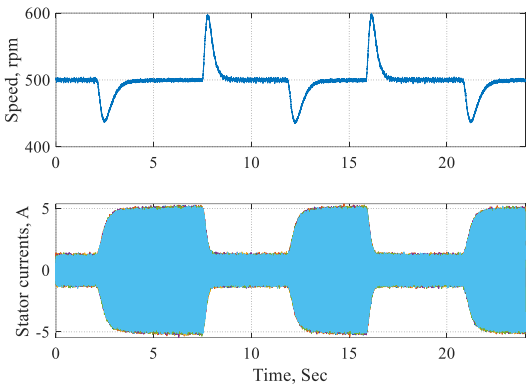

Fig. 24. Step load response of the prototype machine.

B. Charging mode of operation

Besides, the optimized SPM machine has been validated under the charging mode of operation, at which the grid current is 1.93 the stator current, as shown in Fig. 19(b). From Fig. 25, it is clear that the spatial phase shift between the two three-phase winding groups is 150°. Moreover, the grid current and voltage are presented in Fig. 26. Accordingly, the optimized machine can run the charging with unity power factor at the rated current, i.e., maximum charging level. All currents are presented in per unit value with respect to the machine rated current.

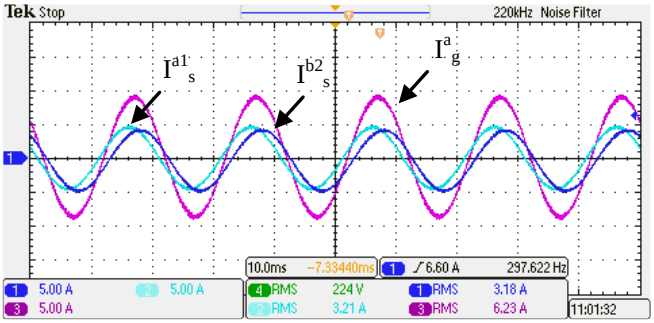

Fig. 25. Stator currents and the grid current under charging.

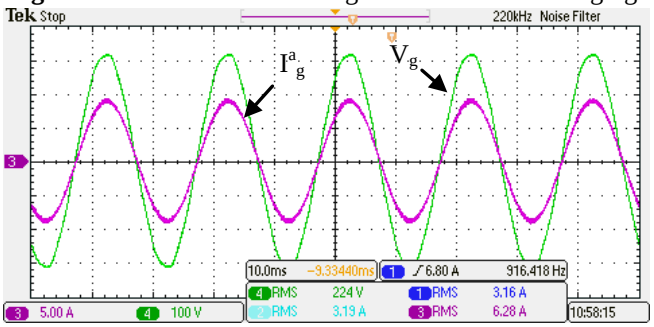

Fig. 26. Grid currents under charging.

To further validate the claimed conclusions, the vibration velocity of the prototype machine is measured under both the asymmetrical six-phase and dual three-phase configurations using a vibration analyzer (SCHENCK® SmartBalancer V2). For the vibration level, the acceptable range of vibration velocity for small machines (class I) is between (0.28-1.8 mm/s) according to ISO 10816 [61]. The vibration level for the prototype machine is 1.717 and 15.458 mm/s for the asymmetrical six-phase and dual three-phase configurations, respectively. Clearly, the vibration level is considered satisfactory and within acceptable limits when the asymmetrical six-phase winding layout is employed. Whilst the dual three-phase configuration is not recommended in the integrated EV charging process.

VI. CONCLUSIONS

This paper presents a thorough comparative analysis of asymmetrical six-phase SPM machines configured with FSCW under both EV propulsion and charging modes. The key topics that are discussed include the torque ripple and core losses under both operational modes, electromagnetic forces and demagnetization capabilities under charging, and the overall cost. These purposes cannot be achieved simultaneously. Therefore, the best compromise has been highlighted for the six motors.

The selected slot/pole combinations are designed and optimized based on the commercial BMW i3 requirements. Simulations show that the selection of the slot/pole combination highly affects the performance of PM machines under both operational modes. The higher the slot/pole combination, the lower the PM volume. Accordingly, the PM loss is considerably reduced under both operational modes, while obtaining the same average torque in the propulsion mode. For higher slot/pole combinations, the torque ripple in both operational modes and the charging core losses are reduced; albeit, the core losses are increased in the propulsion mode. Moreover, the obtained electromagnetic forces support the validity of these slot/pole combination in the charging process. Eventually, a small-scale prototype is constructed to underpin the efficacy of the design optimization process. This paper will provide engineers and researchers a reference that will help them to allocate the suitable slot/pole combination.

VII. ACKNOWLEDGMENTS:

This work was achieved by the financial support of ITIDAs ITAC collaborative funded project under the category type of advanced research projects (ARP) and grant number ARP2020.R29.7.

References

[1] J. Yuan, L. Dorn-Gomba, A. D. Callegaro, J. Reimers, and A. Emadi, "A review of bidirectional on-board chargers for electric vehicles," *IEEE Access*, 2021.

[2] IEA. (2021) Global EV Outlook 2021. Available: https://www.iea.org/reports/global-ev-outlook-2021

[3] M. Y. Metwly, M. S. Abdel-Majeed, A. S. Abdel-Khalik, R. A. Hamdy, M. S. Hamad, and S. Ahmed, "A Review of Integrated On-Board EV Battery Chargers: Advanced Topologies, Recent Developments and Optimal Selection of FSCW Slot/Pole Combination," *IEEE Access*, vol. 8, pp. 85216-85242, 2020.

[4] M. Valente, T. Wijekoon, F. Freijedo, P. Pescetto, G. Pellegrino, and R. Bojoi, "Integrated On-Board EV Battery Chargers: New Perspectives and Challenges for Safety Improvement," in *2021 IEEE Workshop on Electrical Machines Design, Control and Diagnosis (WEMDCD)*, 2021, pp. 349-356: IEEE.

[5] T. Na, X. Yuan, J. Tang, and Q. Zhang, "A review of on-board integrated electric vehicles charger and a new single-phase integrated charger," *CPSS Transactions on Power Electronics and Applications*, vol. 4, no. 4, pp. 288-298, 2019.

[6] C. Shi, Y. Tang, and A. Khaligh, "A Three-Phase Integrated Onboard Charger for Plug-In Electric Vehicles," *IEEE Transactions on Power Electronics*, vol. 33, no. 6, pp. 4716-4725, 2018.

[7] C. Viana and P. W. Lehn, "A Drivetrain Integrated DC Fast Charger with Buck and Boost Functionality and Simultaneous Drive/Charge

Capability," *IEEE Transactions on Transportation Electrification*, pp. 1-1, 2019.
[8] A. Hemeida, M. Y. Metwly, A. S. Abdel-Khalik, and S. Ahmed, "Optimal Design of A 12-Slot/10-Pole Six-Phase SPM Machine with Different Winding Layouts for Integrated On-Board EV Battery Charging," *Energies*, vol. 14, no. 7, p. 1848, 2021.
[9] E. Agamloh, A. von Jouanne, and A. Yokochi, "An overview of electric machine trends in modern electric vehicles," *Machines*, vol. 8, no. 2, p. 20, 2020.
[10] C. Zhou, X. Huang, Z. Li, and W. Cao, "Design Consideration of Fractional Slot Concentrated Winding Interior Permanent Magnet Synchronous Motor for EV and HEV Applications," *IEEE Access*, vol. 9, pp. 64116-64126, 2021.
[11] E. A. Grunditz and T. Thiringer, "Performance Analysis of Current BEVs Based on a Comprehensive Review of Specifications," *IEEE Transactions on Transportation Electrification*, vol. 2, no. 3, pp. 270-289, 2016.
[12] I. Subotic, N. Bodo, and E. Levi, "Single-Phase On-Board Integrated Battery Chargers for EVs Based on Multiphase Machines," *IEEE Transactions on Power Electronics*, vol. 31, no. 9, pp. 6511-6523, 2016.
[13] I. Subotic, V. Katic, N. Bodo, E. Levi, B. Dumnic, and D. Milicevic, "Overview of fast on-board integrated battery chargers for electric vehicles based on multiphase machines and power electronics," *IET Electric Power Applications*, vol. 10, no. 3, pp. 217-229, 2016.
[14] A. Salem and M. Narimani, "A review on multiphase drives for automotive traction applications," *IEEE Transactions on Transportation Electrification*, vol. 5, no. 4, pp. 1329-1348, 2019.
[15] D. TM4. (2020). *increasing inverter power output*. Available: https://www.danatm4.com/technology/power-electronics/multiphase/
[16] I. Subotic, N. Bodo, and E. Levi, "Integration of Six-Phase EV Drivetrains Into Battery Charging Process With Direct Grid Connection," *IEEE Transactions on Energy Conversion*, vol. 32, no. 3, pp. 1012-1022, 2017.
[17] X. Fan, B. Zhang, R. Qu, D. Li, J. Li, and Y. Huo, "Comparative Thermal Analysis of IPMSMs With Integral-Slot Distributed-Winding (ISDW) and Fractional-Slot Concentrated-Winding (FSCW) for Electric Vehicle Application," *IEEE Transactions on Industry Applications*, vol. 55, no. 4, pp. 3577-3588, 2019.
[18] M. Aydin, Y. Demir, E. Yolacan, M. Gulec, and A. El-Refaie, "Design and Validation of an Unconventional 39-Slot PM Synchronous Motor with Asymmetric and Unbalanced AC Windings," *IEEE Journal of Emerging Selected Topics in Power Electronics*, 2021.
[19] V. I. Patel, J. Wang, and S. S. Nair, "Demagnetization assessment of fractional-slot and distributed wound 6-phase permanent magnet machines," *IEEE Transactions on Magnetics*, vol. 51, no. 6, pp. 1-11, 2014.
[20] Y. Demir and M. Aydin, "A novel dual three-phase permanent magnet synchronous motor with asymmetric stator winding," *IEEE Transactions on Magnetics*, vol. 52, no. 7, pp. 1-5, 2016.
[21] A. M. El-Refaie, "Fractional-Slot Concentrated-Windings Synchronous Permanent Magnet Machines: Opportunities and Challenges," *IEEE Transactions on Industrial Electronics*, vol. 57, no. 1, pp. 107-121, 2010.
[22] C. Lu, S. Ferrari, and G. Pellegrino, "Two Design Procedures for PM Synchronous Machines for Electric Powertrains," *IEEE Transactions on Transportation Electrification*, vol. 3, no. 1, pp. 98-107, 2017.
[23] Y.-m. You and K.-y. Yoon, "Multi-Objective Optimization of Permanent Magnet Synchronous Motor for Electric Vehicle Considering Demagnetization," *Applied Sciences*, vol. 11, no. 5, p. 2159, 2021.
[24] H. Wang, S. Liu, S. Wu, L. Guo, and T. Shi, "Optimal Design of Permanent Magnet Structure to Reduce Unbalanced Magnetic Pull in Surface-Mounted Permanent-Magnet Motors," *IEEE Access*, vol. 8, pp. 77811-77819, 2020.
[25] S. Kalt, J. Erhard, and M. Lienkamp, "Electric machine design tool for permanent magnet synchronous machines and induction machines," *Machines*, vol. 8, no. 1, p. 15, 2020.
[26] X. Zhu, W. Wu, L. Quan, Z. Xiang, and W. Gu, "Design and Multi-Objective Stratified Optimization of a Less-Rare-Earth Hybrid Permanent Magnets Motor With High Torque Density and Low Cost," *IEEE Transactions on Energy Conversion*, vol. 34, no. 3, pp. 1178-1189, 2019.
[27] C.-L. Jeong, Y.-K. Kim, and J. Hur, "Optimized design of PMSM with hybrid-type permanent magnet for improving performance and reliability," *IEEE Transactions on Industry Applications*, vol. 55, no. 5, pp. 4692-4701, 2019.
[28] B.-C. Kim, J.-H. Lee, and D.-W. Kang, "A study on the effect of eddy current loss and demagnetization characteristics of magnet division," *IEEE Transactions on Applied Superconductivity*, vol. 30, no. 4, pp. 1-5, 2020.
[29] S. Choi *et al.*, "Fault diagnosis techniques for permanent magnet AC machine and drives—A review of current state of the art," *IEEE Transactions on Transportation Electrification*, vol. 4, no. 2, pp. 444-463, 2018.
[30] H. Chen and C. H. Lee, "Parametric sensitivity analysis and design optimization of an interior permanent magnet synchronous motor," *IEEE Access*, vol. 7, pp. 159918-159929, 2019.
[31] D. Cao, W. Zhao, J. Ji, and Y. Wang, "Parametric Equivalent Magnetic Network Modeling Approach for Multi-Objective Optimization of PM Machine," *IEEE Transactions on Industrial Electronics*, 2020.
[32] A. Hemeida *et al.*, "A simple and efficient quasi-3D magnetic equivalent circuit for surface axial flux permanent magnet synchronous machines," *IEEE Transactions on Industrial Electronics*, vol. 66, no. 11, pp. 8318-8333, 2018.
[33] M. Y. Metwly, A. Hemeida, A. S. Abdel-Khalik, M. S. Hamad, and S. Ahmed, "Design and multi-objective optimization of a 12-slot/10-pole integrated OBC using magnetic equivalent circuit approach," *Machines*, vol. 9, no. 12, p. 329, 2021.
[34] M. Y. Metwly *et al.*, "IoT-Based Supervisory Control of an Asymmetrical Nine-Phase Integrated on-Board EV Battery Charger," *IEEE Access*, vol. 8, pp. 62619-62631, 2020.
[35] Y. Xiao, C. Liu, and F. Yu, "An effective charging-torque elimination method for six-phase integrated on-board EV chargers," *IEEE Transactions on Power Electronics*, vol. 35, no. 3, pp. 2776-2786, 2020.
[36] S. Semsar, T. Soong, and P. W. Lehn, "On-board single-phase integrated electric vehicle charger with V2G functionality," *IEEE Transactions on Power Electronics*, vol. 35, no. 11, pp. 12072-12084, 2020.
[37] J. Gupta, R. Maurya, and S. R. Arya, "Improved power quality on-board integrated charger with reduced switching stress," *IEEE Transactions on Power Electronics*, vol. 35, no. 10, pp. 10810-10820, 2020.
[38] *IEEE Recommended Practice and Requirements for Harmonic Control in Electric Power Systems*, Standard 519-2014, Mar. 2014.
[39] *IEEE Standard for Interconnection and Interoperability of Distributed Energy Resources With Associated Electric Power Systems Interfaces*, Standard 1547-2018, Apr. 2018.
[40] *Inverters, Converters, Controllers and Interconnection System Equipment*, Standard UL 1741, Sep. 2017.
[41] D. Howell, "Current Fiscal Year (2012–2013) Status of the Hybrid and Electric Systems R&D at the US–DOE," *World Electric Vehicle Journal*, vol. 6, no. 3, pp. 502-513, 2013.
[42] S.-O. Plugs, "Vehicle Connectors and Vehicle Inlets—Conductive Charging of Electric Vehicles—Part 1, 2, 3," *IEC Standard*, vol. 62196, pp. 1-176, 2014.
[43] B. Ozpineci, "Oak Ridge National Laboratory annual progress report for the electric drive technologies program," Oak Ridge National Lab.(ORNL), Oak Ridge, TN (United States). Power …2015.
[44] S. O. Edhah, J. Y. Alsawalhi, and A. A. Al-Durra, "Multi-objective optimization design of fractional slot concentrated winding permanent magnet synchronous machines," *IEEE Access*, vol. 7, pp. 162874-162882, 2019.
[45] G. Dajaku, "Advanced multi-phase fractional slot concentrated windings: characteristics and potentials," *Electrical Engineering*, vol. 103, no. 1, pp. 397-406, 2021.
[46] S. Liu and J. Huang, "Multi-objective optimization of a spoke-type permanent magnet motor with fractional-slot concentrated windings for EVs," *COMPEL-The international journal for computation mathematics in electrical electronic engineering*, 2021.
[47] W. Zhao, S. Zhu, J. Ji, G. Liu, and Y. Mao, "Analysis and Reduction of Electromagnetic Vibration in Fractional-Slot Concentrated-Windings PM Machines," *IEEE Transactions on Industrial Electronics*, 2021.
[48] V. I. Patel, J. Wang, W. Wang, and X. Chen, "Six-phase fractional-slot-per-pole-per-phase permanent-magnet machines with low space harmonics for electric vehicle application," *IEEE Transactions on Industry Applications*, vol. 50, no. 4, pp. 2554-2563, 2014.
[49] S. Huang, J. Luo, F. Leonardi, and T. A. Lipo, "A general approach to sizing and power density equations for comparison of electrical machines," *IEEE Transactions on Industry Applications*, vol. 34, no. 1, pp. 92-97, 1998.
[50] P. Ponomarev, "Tooth-coil permanent magnet synchronous machine design for special applications," 2013.
[51] Dober. (2021). *Lithium-Ion Battery Packs & Methods of Cooling Them*. Available: https://www.dober.com/electric-vehicle-cooling-systems#electric_vehicle_thermal_management_system

[52] M. Martínez-Iranzo, J. M. Herrero, J. Sanchis, X. Blasco, and S. García-Nieto, "Applied Pareto multi-objective optimization by stochastic solvers," *Engineering applications of artificial intelligence*, vol. 22, no. 3, pp. 455-465, 2009.
[53] X. Zhu, Z. Shu, L. Quan, Z. Xiang, and X. Pan, "Multi-Objective Optimization of an Outer-Rotor V-Shaped Permanent Magnet Flux Switching Motor Based on Multi-Level Design Method," *IEEE Transactions on Magnetics*, vol. 52, no. 10, pp. 1-8, 2016.
[54] X. Zhu, D. Fan, Z. Xiang, L. Quan, W. Hua, and M. Cheng, "Systematic multi-level optimization design and dynamic control of less-rare-earth hybrid permanent magnet motor for all-climatic electric vehicles," *Applied Energy*, vol. 253, 2019.
[55] J. Yin, X. Zhu, L. Quan, C. Zhang, and Z. Xiang, "Comprehensive multi-objective scalarisation optimisation of a permanent magnet machine with correlation parameters stratified method," *IET Electric Power Applications*, vol. 11, no. 1, pp. 72-79, 2017.
[56] K. Meessen, J. Paulides, and E. Lomonova, "Force calculations in 3-D cylindrical structures using Fourier analysis and the Maxwell stress tensor," *IEEE Transactions on Magnetics*, vol. 49, no. 1, pp. 536-545, 2012.
[57] W. Li, G. Feng, C. Lai, Z. Li, J. Tian, and N. C. Kar, "Demagnetization analysis of interior permanent magnet machines under integrated charging operation," *IEEE Transactions on Industry Applications*, vol. 55, no. 5, pp. 5204-5213, 2019.
[58] A. Hemeida, "Electromagnetic and thermal design of axial flux permanent magnet synchronous machines," Ghent University, 2017.
[59] Z. Wang, J. Chen, M. Cheng, and K. Chau, "Field-oriented control and direct torque control for paralleled VSIs fed PMSM drives with variable switching frequencies," *IEEE Transactions on Power Electronics*, vol. 31, no. 3, pp. 2417-2428, 2016.
[60] M. S. Abdel-Majeed, A. Shawier, A. S. Abdel-Khalik, M. S. Hamad, M. M. Sedky, and N. A. Elmalhy, "General Current Control of Six-Phase-Based Non-Isolated Integrated On-Board Charger with Low Order Harmonic Compensation," *Sustainability*, vol. 14, no. 3, p. 1088, 2022.
[61] J. M. Robichaud and "Reference standards for vibration monitoring and analysis," *Bretech Engineering Ltd*, vol. 70, 2009.

Mohamed Y. Metwly (GS'21) received the B.Sc. degree in electrical engineering from Alexandria University, Alexandria, Egypt, in 2018. He is currently a researcher at Smart-CI, Alexandria University, Alexandria, Egypt. His current research interests include machine design, battery chargers, electric vehicles, renewable energy systems, and multi-objective optimization.

Mohamed Ahmed received the B.Sc. degree in Electrical Engineering from Alexandria University, Alexandria, Egypt, in 2016. He is currently a Teaching Assistant with the Mathematics and Applied Physics Department, Faculty of Engineering, Alexandria University, Alexandria, Egypt. His current research interest includes renewable energy, power system control, and power electronics.

Ahmed Hemeida received the B.Sc. and M.Sc. degrees from the department of electrical power and engineering, Cairo University, Egypt, in 2009 and 2012, respectively. In 2017, he obtained his PhD degree in the Department of Electrical Energy, Metals, Mechanical Constructions and Systems, Ghent University, Belgium. He worked afterwards as a Postdoctoral Research Assistant with the department of electrical Engineering in Aalto University in Finland. He is currently working as an assistant professor in the electrical engineering department in Cairo University, Egypt. His research interests include the modeling, control and design of electrical machines.

Ayman S. Abdel-Khalik (SM'12) received the B.Sc. and M.Sc. degrees in electrical engineering from Alexandria University, Alexandria, Egypt, in 2001 and 2004, respectively, and the Ph.D. degree in electrical engineering from Alexandria University, and Strathclyde University, Glasgow, U.K., in 2009, under a dual channel program. He is currently a Professor with the Electrical Engineering Department, Faculty of Engineering, Alexandria University, Alexandria, Egypt. He serves as an Associate Editor of IEEE Transactions on Industrial Electronics and IET Electric Power Applications Journal. Also, he serves as the Executive Editor of Alexandria Engineering Journal. His current research interests include electrical machine design and modelling, electric drives, energy conversion, and renewable energy.

Mostafa Hamad (SM'19) obtained the B.Sc. and M.Sc. degrees in Electrical Engineering from Alexandria University, Alexandria, Egypt, in 1999 and 2003, respectively, and the Ph.D. degree in Electrical Engineering from Strathclyde University, Glasgow, U.K., in 2009.

Currently he is a Professor in the Department of Electrical and Control Engineering, College of Engineering and Technology, Arab Academy for Science, Technology and Maritime Transport (AASTMT), Alexandria, Egypt. His research interests include power electronics applications in power quality, electric drives, distributed generation, HVDC transmission systems, and renewable energy.

Anouar Belahcen (M13-SM15) was born in Morocco in 1963. He received the M.Sc. (Tech.) and Doctor (Tech.) degrees from Aalto University (former Helsinki University of Technology), Finland, in 1998, and 2004, respectively. He is now Professor of Power and Energy at Aalto University, Finland. His research interest are numerical modelling of electrical machines, characterization and modelling of magnetic materials, coupled magneto-mechanical problems, magnetic forces, magnetostriction, and fault diagnostics of electrical machines. Since 2020, Anouar Belahcen is the vice dean for education at the school of Electrical Engineering at Aalto University.

Shehab Ahmed (SM'12) received the B.Sc. degree in electrical engineering from Alexandria University, Alexandria, Egypt, in 1999, and the M.Sc. and Ph.D. degrees from the Department of Electrical and Computer Engineering, Texas A&M University, College Station, TX, USA, in 2000 and 2007, respectively. He was with Schlumberger Technology Corporation, Houston, TX, USA, from 2001 to 2007, developing downhole mechatronic systems for oilfield service products. He was with Texas A&M University at Qatar from 2007 to 2018. He is currently Professor and Program Chiar of the Electrical and Computer Engineering program in the CEMSE Division at King Abdullah University of Science and Technology (KAUST), Saudi Arabia. His research interests include mechatronics, solid-state power conversion, and electric machines.

Noha Elmalhy received the B.Sc. and M.Sc. degrees in electrical engineering from Alexandria University, Alexandria, Egypt, in 2005 and 2010, respectively, and the Ph.D. degree in electrical engineering from Alexandria University in 2017. She is currently a Lecturer with the Electrical Engineering Department, Faculty of Engineering, Alexandria University, Alexandria, Egypt. Her current research interests include electrical machine and drives, energy conversion, and renewable energy.